arXiv:2506.16377v1 [physics.geo-ph] 19 Jun 2025

Frequency Differences between Clocks on the Earth and the Moon

Mingyue Zhang, Jürgen Müller
Institute of Geodesy (IfE), Leibniz University Hannover, Schneiderberg 50, 30167 Hannover, Germany

Sergei M. Kopeikin
Department of Physics & Astronomy, University of Missouri, 322 Physics Bldg., Columbia, Missouri 65211, USA

Based on general relativity, clock comparisons enable the determination of the gravity potential relative to a stable reference. Lunar surface clocks, owing to the Moon's low-noise conditions, high orbital stability, and broad Earth visibility, are promising reference clocks for global-scale comparisons between terrestrial clocks. Meanwhile, the need for an independent lunar time system—driven by future lunar navigation—requires maintaining links to terrestrial standards. This Letter simulates fractional frequency differences between Earth (E) and Moon (L) clocks by modeling three key time transformations: proper-to-coordinate time for E-clocks and for L-clocks (both linked to the local gravity potential), and the coordinate time relation between Earth and Moon. Signal propagation effects are not addressed. Gravity potential differences impact observations at the 10^{-10} level, and the coordinate time ratio at 10^{-11}. Contributions from static, tidal, and non-tidal potentials, body self-rotation, and different celestial bodies are evaluated.

Introduction—As implied by general relativity, clock frequency measurements can be used to determine gravity potential [1, 2]. This concept, known as chronometric geodesy, supports various terrestrial studies, e.g., geopotential investigations [3–5], sea level monitoring [6], height system unification [7–9], and relativity tests [10]. These rely on frequency differences relative to a reference clock. Earth- and satellite-based clocks can serve this role but are limited by environmental noise, orbital instability, and restricted visibility [11]. In contrast, lunar surface clocks benefit from a stable orbit, low disturbance, and wide Earth visibility, making them promising candidates for global-scale chronometric applications.

In parallel, clock-based timekeeping underpins future lunar navigation. Projects like ESA's Moonlight [12] and NASA's LCRNS [13] highlight the need for a dedicated lunar time scale [14], prompting frameworks for its definition and relation to terrestrial standards [15–17].

To support lunar timekeeping and chronometric geodesy, this Letter quantifies the fractional frequency differences between clocks on Earth and the Moon via site-specific gravity potential models and coordinate-time transformations. In contrast to prior clock-based gravity and lunar time studies—focused on Earth-only systems and theoretical frameworks, respectively—this work simulates a practical Earth-Moon configuration using surface stations. It expands chronometric modeling beyond the terrestrial domain and quantifies how gravity potential components and celestial bodies affect the frequency difference and coordinate-time relation. This dual-perspective analysis advances lunar timekeeping and gravity sensing, supporting future Earth–Moon timing and chronometric applications.

Proper time and coordinate time—Proper time is the time measured by a clock in its own rest frame, while coordinate time is a variable used in a specific reference system to describe the temporal ordering of events [18, 19]. The coordinate time of the Earth-centered local inertial frame, i.e., the Geocentric Celestial Reference System (GCRS), is Geocentric Coordinate Time ($u \equiv$ TCG) [20]. Analogous to GCRS and TCG, Kopeikin and Kaplan [16] defined the Lunar Celestial Reference System (LCRS) and its time counterpart, Lunar Coordinate Time ($s \equiv$ TCL), for the Moon-centered local inertial frame.

For a clock at rest on the Earth's surface (E-clock), with the gravity potential W_E, the relation between its proper time τ_E and TCG is [19]

$$\frac{d\tau_E}{du_E} = 1 - \frac{W_E}{c^2} + O(c^{-4}) \,, \tag{1}$$

where c is the speed of light, and u_E denotes TCG calculated at the point of the location of E-clock. Similarly, for a clock at rest on the lunar surface (L-clock), with the gravity potential W_L, its proper time τ_L and TCL are related by [16]

$$\frac{d\tau_L}{ds_L} = 1 - \frac{W_L}{c^2} + O(c^{-4}) \,, \tag{2}$$

where s_L denotes TCL calculated at the point of the location of L-clock.

Simulation method and settings—According to the gravitational redshift formula [21, 22], the proper frequency f_E measured by an E-clock differs from the frequency f_L measured by an L-clock for the same electromagnetic signal. The frequency is inversely proportional to the period of oscillation measured by the clock, with $f_E = (d\tau_E)^{-1}$ and $f_L = (d\tau_L)^{-1}$. The electromagnetic signal is used to synchronize the two clocks, and the fractional frequency difference between the two clocks is given by equation $\Delta f/f_L = d\tau_L/d\tau_E - 1$ with

$\Delta f = f_E - f_L$, where

$$\frac{d\tau_L}{d\tau_E} = \frac{d\tau_L}{ds_L}\frac{ds_L}{du_L}\frac{du_L}{du_E}\frac{du_E}{d\tau_E} \ . \tag{3}$$

The derivatives $d\tau_L/ds_L$ and $du_E/d\tau_E$ are computed from Eqs. (1) and (2). The term ds_L/du_L is based on Kopeikin and Kaplan [16]. du_L/du_E—the derivative calculated along the electromagnetic signal path for clock synchronization—is derived by solving the equations of light propagation in the GCRS [23], with its errors carefully investigated in Liu *et al.* [24]. Here du_L/du_E is assumed to be unity for simplicity and will be addressed in future work.

Based on Eqs. (1)–(3), the fractional frequency difference between E- and L-clock is:

$$\frac{\Delta f}{f_L} = \frac{W_E - W_L + F}{c^2} + O(c^{-4}) \ . \tag{4}$$

Here the ratio $F/c^2 = ds_L/du_L - 1$. Modern optical clocks, with a fractional frequency uncertainty of 10^{-18}, can detect gravity potential changes of ~ 0.1 m^2/s^2, corresponding to ~ 1 cm in height on Earth [19, 25, 26] and ~ 6 cm on the Moon, making them vital for high-precision geodesy [19]. The simulated observation uncertainty is thus set to 10^{-18} and all effects contributing around or above this level are included (see following sections). E-clocks are assumed to be at six lunar laser ranging (LLR) stations: LURE, APOLLO, MLRS2, OCA, WLRS, and MLRO (Fig. 1(a)) and L-clocks at five LLR retro-reflectors: A11, A14, A15, L17, and L21 (Fig. 1(b)). Hourly observations are simulated for 2009 due to the better availability of GNSS data for determining the E-clocks' gravity potential.

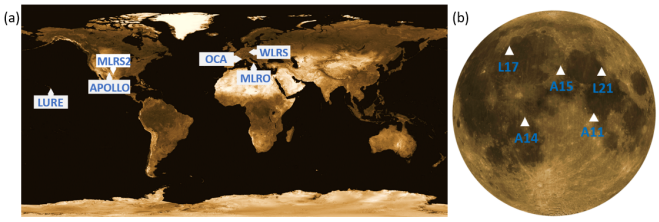

FIG. 1. (a) Assumed E-clocks' locations, and (b) L-clocks' locations.

Gravity potential—The gravity potential $W = \Phi + V$ of a celestial body is the sum of the centrifugal potential Φ from rotation and gravitational potential $V = V_{\rm static} + \delta V$, which includes a dominant static part $V_{\rm static}$ and a time-varying component δV. For a point with radial distance r, polar distance θ, and longitude λ, $V_{\rm static}$ is calculated from the normalized Stokes coefficients $\bar{C}_{nm}$ and $\bar{S}_{nm}$ (degree n and order m) based on a static gravity field model and the normalized associated Legendre function $\bar{P}_{nm}(\cos\theta)$:

$$V_{\rm static} = \frac{GM}{r}\left[1 + \sum_{n=2}^{\infty}\left(\frac{a}{r}\right)^n \sum_{m=0}^{n} \bar{P}_{nm}(\cos\theta) \times \left(\bar{C}_{nm}\cos m\lambda + \bar{S}_{nm}\sin m\lambda\right)\right], \tag{5}$$

where G, M, and a represent the gravitational constant, the body's mass and the equatorial radius, respectively [27]. The time-varying component, calculated as an effective potential variation, $\delta V = \sum_i (1 + k_i + h_i)\,\delta V_i$ is a sum of harmonics. δV_i represents the direct potential effects of various tidal and non-tidal geophysical forcings, e.g., tidal forces, the attraction of the moving ocean water or air masses, the centrifugal effect of polar motion and hydrological signals. The (load) Love numbers k_i and h_i, varying with degree n and order m, characterize the body's response to these forcings, including the induced gravitational potential change and surface deformations [3–5, 28, 29]. In our simulation, we consider both tidal and non-tidal variations in δV for the Earth, and only tidal effects for the Moon. The centrifugal potential Φ is determined by the body's angular velocity $\boldsymbol{\omega}$ and the clock's position $\boldsymbol{r}$ on the body surface:

$$\Phi = \frac{1}{2}(\boldsymbol{\omega} \times \boldsymbol{r})^2 \ . \tag{6}$$

E-clocks

Considering the Moon's orbital period, the daily Earth gravity field model ITSG-Grace2018 is used to represent both static and non-tidal temporal potential (hydrological, cryospheric, and glacial isostatic adjustment signals) [30, 31], denoted as $V_{\rm ITSG}$. The AOD1B RL06 time series [32] is used to model the potential variation $V_{\rm AOD}$ caused by non-tidal atmospheric and oceanic mass variability. To fully evaluate effective potential variations from the non-tidal part, surface deformation effects $V_{\rm GNSSh} = \sum_i h_i \delta V_i$ are calculated using daily GNSS displacement δH [33] from selected stations (MAUI, WTZR, GRAS [34], MDO1, P027 [35], MATE) and gravity acceleration g, simplified as $\sum_i h_i \delta V_i = g\delta H$ [4, 5]. Effective potential variations of solid Earth tides $V_{\rm EP-SET}$ and pole tides $V_{\rm EP-SEP}$ are computed with the modified tool ETERNA 3.4 [36], and ocean tide loading $V_{\rm EP-OTL}$ with SPOTL 3.3.0.2 [37, 38]. Other tidal factors, like ocean pole and atmospheric tides, are ignored. Earth's angular velocity for the centrifugal potential Φ_E is derived from IERS EOP C04 LOD data [39] with corrections from ocean tides and libration [20].

The contributions of individual components of the E-clock gravity potential W_E—Φ_E, $V_{\rm ITSG}$, $V_{\rm AOD}$, $V_{\rm GNSSh}$, $V_{\rm EP-SET}$, $V_{\rm EP-OTL}$, $V_{\rm EP-SEP}$—to E–L clock observations are evaluated as their values divided by c^2. Their approximate values in Tab. I are calculated using the full model series of LOD (1962-2025), ITSG

(2002–2017), AOD (1976–2025) and GNSS (station-dependent) with the latter three restricted to ITSG's timespan (2002–2017). The dominant terms are $V_{\rm ITSG}$ and Φ_E, about 6.96×10^{-10} and from 5.14×10^{-13} to 10.49×10^{-13} for the six stations, while the smallest terms $V_{\rm EP-SEP}$ and $V_{\rm AOD}$ are around 1×10^{-18}. Based on the available uncertainties of ITSG and GNSS models, $V_{\rm ITSG}/c^2$ and $V_{\rm GNSSh}/c^2$ uncertainties at all six clock locations are calculated over the full model timespans. Except for a few epochs (outside 2009) of the E-clocks at OCA and MLRO for the GNSS model slightly exceeding 1×10^{-18}, all values remain within this limit, including their combined uncertainty.

TABLE I: W_E element effects on $\Delta f/f_L$ for E-clocks' locations. Starred columns vary with time and station, rounded for presentation.

Station	$V_{\rm ITSG}/c^{2*}$ $\times 10^{-10}$	Φ_E/c^{2*} $\times 10^{-13}$	$V_{\rm GNSSh}/c^2$ $\times 10^{-17}$	$V_{\rm EP-SET}/c^2$ $\times 10^{-17}$	$V_{\rm EP-OTL}/c^2$ $\times 10^{-18}$	$V_{\rm EP-SEP}/c^2$ $\times 10^{-19}$	$V_{\rm AOD}/c^2$ $\times 10^{-19}$
LURE	6.96	10.49	-1.5 to -0.8	-2.4 to 4.7	-8.5 to 10.3	-5.9 to 6.0	-6.6 to 5.5
APOLLO		8.48	-8.3 to -7.8	-2.4 to 4.6	-3.8 to 4.2	-7.7 to 8.2	-10.0 to 7.7
MLRS2		8.87	-5.8 to -5.0	-2.4 to 4.6	-3.3 to 3.8	-7.4 to 7.9	-10.0 to 7.7
WLRS		5.14	-0.5 to 0.1	-2.4 to 3.6	-3.3 to 2.0	-8.8 to 8.9	-15.0 to 11.8
OCA		6.27	-3.8 to -3.1	-2.4 to 4.0	-4.0 to -3.1	-8.8 to 9.0	-9.7 to 9.1
MLRO		6.91	-7.7 to -6.1	-2.4 to 4.3	-2.8 to 2.3	-8.9 to 8.9	-10.0 to 9.6

L-clocks

Several lunar gravity field models (GFMs) [40] from the NASA's GRAIL mission [41] were compared to compute the lunar static gravitational potential $V_{\rm GRAIL}$. Using normalized Stokes coefficients $\bar{C}_{nm}$ and $\bar{S}_{nm}$ and their uncertainties $\delta\bar{C}_{nm}$ and $\delta\bar{S}_{nm}$, Fig. 2 highlights, for each degree n, the number of order m with insignificant coefficients, i.e., where $\delta\bar{C}_{nm} > |\bar{C}_{nm}|$ or $\delta\bar{S}_{nm} > |\bar{S}_{nm}|$ or both. Given model stability, calculation reliability, and the need to retain maximum information, the models are truncated to the maximum degrees in the third column "Max n (used)" of Tab. II. Based on $V_{\rm GRAIL}/c^2$ uncertainties in the same table, model GL0900D was selected.

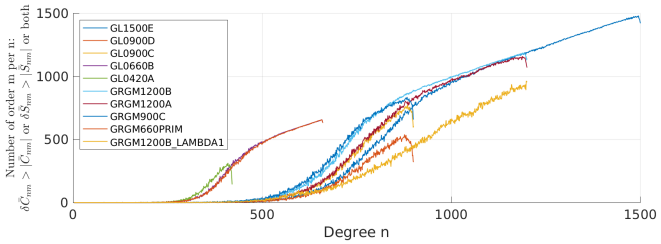

FIG. 2. Comparison of lunar GFMs.

The lunar tidal potential $V_{\rm LTP}$ at a position p_m on the Moon with spherical coordinates $(r_{p_m}, \theta_{p_m}, \lambda_{p_m})$ resulting from a tide-generating body b with mass M_b and coordinates $(r_b, \theta_b, \lambda_b)$ at time t can be calculated by [42]

TABLE II: $V_{\rm GRAIL}/c^2$ uncertainties for L-clocks' locations using different lunar GFMs.

Lunar GFMs	Max n (model)	Max n (used)	$\frac{V_{\rm GRAIL}}{c^2}$ uncertainty $\times 10^{-19}$ A11	L21	A14	A15	L17
GL0420A	420	250	2.5	3.0	2.3	2.7	3.0
GL0666B	660	300	4.7	5.2	4.1	4.5	5.0
GRGM660PRIM	660	300	5.1	5.7	4.5	5.0	5.7
GRGM900C	900	500	5.9	6.5	4.7	5.2	5.3
GL0900C	900	500	3.1	3.4	2.5	2.7	2.8
GL0900D	**900**	**500**	**1.8**	**2.0**	**1.5**	**1.6**	**1.6**
GRGM1200A	1200	500	3.0	3.4	2.4	2.9	2.8
GRGM1200B	1200	500	3.0	3.4	2.4	2.9	3.1
GRGM1200Blambda1	1200	500	3.0	3.4	2.4	2.9	3.1
GL1500E	1500	500	2.1	2.2	1.7	1.8	1.8

$$V_{\rm LTP} = \frac{GM_b}{r_b} \sum_{n=2}^{\infty} \left(\frac{r_{p_m}}{r_b}\right)^n \frac{1}{2n+1} \sum_{m=0}^{n} \bar{P}_{nm}(\cos\theta_{p_m}) \times \bar{P}_{nm}(\cos\theta_b) \cdot \cos\left(m\lambda_{p_m} - m\lambda_b\right). \quad (7)$$

The bodies' ephemerides are generated by numerically integrating a DE440-based dynamical model [43] in the LLR software LUNAR [44–48] with lunar initial states and other parameters fitted to over 53 years of LLR data. Given the clock uncertainty of 10^{-18}, only Earth and Sun contributions up to degrees $n = 3$ and 2 are sufficient; higher degrees and other bodies are negligible. For the lunar effective tidal potential $V_{\rm ELTP}$, degree-2 Love numbers (k_{l2} and h_{l2}) and the associated tidal time delay are considered.

The angular velocity of the lunar mantle $\boldsymbol{\omega}_L$ is integrated concurrently with the ephemerides, based on its time derivative [49, Eq. (34)], to calculate the lunar centrifugal potential Φ_L.

Tab. III summarizes the contributions of W_L elements to $\Delta f/f_L$: $V_{\rm GRAIL}/c^2$ about 3.14×10^{-11}, Φ_L/c^2 around 1×10^{-16}, and $V_{\rm ELTP}/c^2$ ranging from -0.3×10^{-16} to 2.6×10^{-16} for the five reflectors. Variations in $V_{\rm ELTP}/c^2$ and Φ_L/c^2 are derived from over 50 years of ephemerides and a $\boldsymbol{\omega}_L$ series. In $V_{\rm ELTP}/c^2$, the dominant contribution comes from Earth (up to degree 3), while effects from the Sun (degree 2) and lunar response (k_{l2} and h_{l2} part) are smaller, varying from -0.7×10^{-18} to 1.4×10^{-18} and -5.0×10^{-18} to 0.6×10^{-18}, respectively. Earth degree 3 alone contributes -0.6×10^{-18} to 1.2×10^{-18}.

TABLE III: W_L element effects on $\Delta f/f_L$ for L-clocks' locations. The starred column varies with time, rounded for presentation.

Reflector	$\frac{V_{\rm GRAIL}}{c^2} \times 10^{-11}$	$\frac{\Phi_L}{c^2}^* \times 10^{-16}$	$\frac{V_{\rm ELTP}}{c^2} \times 10^{-16}$
A11	3.1436	1.19	1.26 to 2.35
L21	3.1450	0.96	0.28 to 1.63
A14	3.1420	1.18	1.48 to 2.61
A15	3.1436	0.96	1.07 to 2.41
L17	3.1444	0.73	-0.31 to 0.94

Earth-Moon coordinate time ratio—We analyze the Earth-Moon time ratio F/c^2 in Eq. (4) using two approaches. First, the relationships between Barycentric Coordinate Time ($t \equiv$ TCB) and Terrestrial Coordinate

Time ($u \equiv$ TCG), and between TCB and Lunar Coordinate Time ($s \equiv$ TCL) follow [16, Eqs. (1) and (2)]. At the L-clock's location, $F/c^2 = (ds_L/dt)(dt/du_L) - 1$. By computing the derivatives, we obtain:

$$\frac{F}{c^2} = -\frac{1}{c^2}\Big[\sum_{A\neq L}\frac{GM_A}{r_{LA}} - \sum_{A\neq E}\frac{GM_A}{r_{EA}} + \frac{v_L^2 - v_E^2}{2} + \boldsymbol{a}_L\cdot\boldsymbol{r}_{pL} + \boldsymbol{v}_L\cdot\boldsymbol{v}_{pL} - \boldsymbol{a}_E\cdot\boldsymbol{r}_{pE} - \boldsymbol{v}_E\cdot\boldsymbol{v}_{pE}\Big] + O(c^{-4})\,. \tag{8}$$

We use BCRS coordinates $\boldsymbol{x}_E$, $\boldsymbol{x}_L$, $\boldsymbol{x}_p$ of the Earth, Moon and L-clock, and their velocities $\boldsymbol{v}_E$, $\boldsymbol{v}_L$, $\boldsymbol{v}_p$, respectively. We denote $\boldsymbol{r}_{pE} = \boldsymbol{x}_p - \boldsymbol{x}_E$, $\boldsymbol{r}_{pL} = \boldsymbol{x}_p - \boldsymbol{x}_L$ and $\boldsymbol{v}_{pE} = \boldsymbol{v}_p - \boldsymbol{v}_E$, $\boldsymbol{v}_{pL} = \boldsymbol{v}_p - \boldsymbol{v}_L$. The BCRS accelerations of the Earth and Moon are $\boldsymbol{a}_E$ and $\boldsymbol{a}_L$. The distances r_{EA} and r_{LA} are between body A with mass M_A and Earth, and between body A and Moon. Second, we use a theoretical relation between TCG and TCL derived by Kopeikin and Kaplan [16, Eq. (12)], which does not rely on using the BCRS as an intermediate coordinate system. By computing the derivative from this relation and taking into account terms of the second and third order of the tidal potential U, we obtain:

$$\frac{F}{c^2} = -\frac{1}{c^2}\Big(\boldsymbol{a}_{LE}\cdot\boldsymbol{r}_{pL} + \boldsymbol{v}_{LE}\cdot\boldsymbol{v}_{pL} + \frac{v_{LE}^2}{2} + \frac{GM_E}{r_{LE}} - \frac{2GM_L}{r_{LE}} + U_2 + U_3\Big) + O(c^{-4})\,, \tag{9}$$

where $\boldsymbol{r}_{LE} = \boldsymbol{x}_L - \boldsymbol{x}_E$, $\boldsymbol{v}_{LE} = \boldsymbol{v}_L - \boldsymbol{v}_E$ and $\boldsymbol{a}_{LE} = \boldsymbol{a}_L - \boldsymbol{a}_E$, and

$$U_2 = \sum_{A\neq E,L}\frac{GM_A}{2r_{EA}}\left(\frac{r_{LE}}{r_{EA}}\right)^2\left(3\cos^2\psi_{LA} - 1\right)\,, \tag{10}$$

$$U_3 = \sum_{A\neq E,L}\frac{GM_A}{2r_{EA}}\left(\frac{r_{LE}}{r_{EA}}\right)^3\left(5\cos^3\psi_{LA} - 3\cos\psi_{LA}\right)\,. \tag{11}$$

Here, $\cos\psi_{LA} = \boldsymbol{n}_{AE}\cdot\boldsymbol{n}_{LE}$, where ψ_{LA} is the angle between the two unit vectors $\boldsymbol{n}_{AE}$ and $\boldsymbol{n}_{LE}$, which are directed from Earth's geocenter to body A and the Moon, respectively.

Barycentric Dynamical Time (TDB) is used in LUNAR for calculating the ephemerides, while the quantities in Eqs. (8) and (9) are TCB-compatible. TDB is scaled to TCB by the factor $(1 - L_B)$, where $L_B = 1.550519768 \times 10^{-8}$ [20] along with corresponding rescaling of spatial coordinates and body masses. This procedure leaves Eq. (8) and Eq. (9) unchanged [50].

Due to mutual interactions among bodies, the accelerations, velocities, and positions in Eqs. (8) and (9) inherently reflect combined effects. As a result, the isolated contribution of a single body cannot be uniquely extracted. We therefore evaluate the effect of a body only based on the terms in which it appears directly in the equations. For Earth and Moon, these include the acceleration-, velocity-, and gravitational potential-related terms in both Eqs. (8) and (9), but the two equations provide different expressions for them. For other bodies, only the potential terms in Eq. (8), and the tidal terms in Eq. (9) are involved.

Tab. IV presents the effects on F/c^2 in Eqs. (8) and (9) from the ten major solar-system bodies: Earth, Moon, Sun, and the other seven planets. The effect of each body differs between the two equations due to the differences in the terms used. However, in both cases, the largest contributions to F/c^2 come from the Earth, Moon, and Sun, followed by Jupiter (the most massive solar-system planet) and Venus (with the orbit closest to the Earth's); the other planets contribute less. Compared to Eq. (8), Venus contributes more than Jupiter in Eq. (9), as the distance weights more than mass in tidal potentials. The same holds for Mars and Saturn.

Despite the differences in individual contributions, the total effect from all bodies remains consistent between the two equations. For the 10^{-18} clock uncertainty, Eq. (8) requires all ten major solar-system bodies. In contrast, Eq. (9) matches Eq. (8), at the 10^{-18} level using only Earth, Moon, and Sun, with occasional differences exceeding 1×10^{-17} (Fig. 3(a)). Adding Venus and Jupiter further decreases the overall differences (Fig. 3(b)). While both equations identify the Earth, Moon, and Sun as dominant contributors, Eq. (9) places even greater emphasis on them. The F/c^2 differences among L-clock sites reach the 10^{-15} level, computed using either Eq. (8) or Eq. (9) .

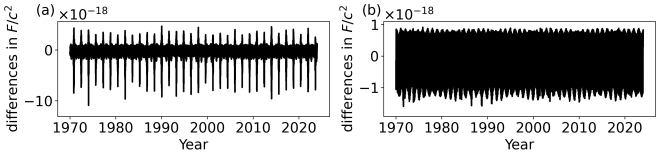

FIG. 3. Differences in F/c^2 over 50 years for the L-clock at A15 between Eq. (8) (10 major bodies) and Eq. (9), considering (a) Earth, Moon, and Sun, and (b) Earth, Moon, Sun, Venus, and Jupiter.

Compared to [16, Eq. (12) and its variant Eq. (29)], our Eq. (9), the time derivative of [16, Eq. (12)], further extends the tidal potential to the third order. The term U_3/c^2 reaches the 10^{-16} level in F/c^2 at all L-clock sites (see Fig. 4 for the L-clock at A15) and must be included to remain compatible with a 10^{-18} clock uncertainty. Higher orders can be ignored. The analytic solution of [16, Eq. (29)] in [16, Eq. (72)] relies on a simplified Keplerian model and neglects perturbations from the major planets, whereas our approach uses numerically integrated ephemerides to capture the full multi-body dynamics of the solar system.

Lunar librations affect the relative rate of the lunar clock with respect to the Earth clock and must be taken

TABLE IV: Effects of solar-system bodies on F/c^2. Each body's effect differs between Eqs. (8) and (9), but the total effect from all bodies remains consistent (Fig. 3(b)).

Eq.	Earth+Moon	Sun	Jupiter	Venus	Saturn	Mars	Mercury	Uranus	Neptune
(8)	$(-4.4\,\text{to}\,1.2)\times10^{-11}$	$(-2.8\,\text{to}\,2.8)\times10^{-11}$	$(-1.6\,\text{to}\,1.6)\times10^{-15}$	$(-9.2\,\text{to}\,9.0)\times10^{-16}$	$(-1.2\,\text{to}\,1.2)\times10^{-16}$	$(-5.8\,\text{to}\,5.8)\times10^{-17}$	$(-1.5\,\text{to}\,1.4)\times10^{-17}$	$(-3.9\,\text{to}\,3.8)\times10^{-18}$	$(-1.6\,\text{to}\,1.6)\times10^{-18}$
(9)	$(-1.9\,\text{to}\,-1.6)\times10^{-11}$	$(-7.7\,\text{to}\,3.8)\times10^{-14}$	$(-1.1\,\text{to}\,0.6)\times10^{-18}$	$(-9.2\,\text{to}\,4.6)\times10^{-18}$	$(-4.0\,\text{to}\,2.0)\times10^{-20}$	$(-4.0\,\text{to}\,2.2)\times10^{-19}$	$(-7.2\,\text{to}\,3.5)\times10^{-20}$	$(-6.0\,\text{to}\,3.0)\times10^{-22}$	$(-1.5\,\text{to}\,0.8)\times10^{-22}$

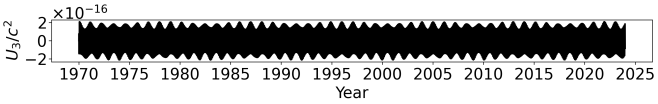

FIG. 4. Effect of the third-order tidal potential U_3/c^2 in Eq. (9) over 50 years for the L-clock at A15, from Sun, Venus, and Jupiter.

into account [16]. In LLR, geometric libration is implicitly included via ephemerides and light-time models, as it modulates the Earth–Moon distance. Physical libration is explicitly modeled in transforming coordinates from the lunar body-fixed frame to the BCRS. Accordingly, Eqs. (8) and (9) incorporate libration effects via the L-clocks' positions and Earth–Moon distance derived from ephemerides.

Results—Based on Tabs. I and III, the effects on $\Delta f/f_L$ from the gravity potentials of Earth clocks W_E/c^2 and Moon clocks W_L/c^2 are on the order of 10^{-10} and 10^{-11}, respectively. Their differences $(W_E - W_L)/c^2$ are at the 10^{-10} level (see Fig. 5(a) for the E-clock at APOLLO and L-clock at A15 in 2009). Results for F/c^2 from Eqs. (8) and (9) are highly consistent, both indicating values at the 10^{-11} level. Fig. 5(b) shows the result of Eq. (8) for the L-clock at A15 in 2009, using the reception time series based on the signal from the E-clock at APOLLO. Fig. 5(c) shows the simulated fractional frequency differences in 2009 for the E- and L-clocks assumed at APOLLO and A15.

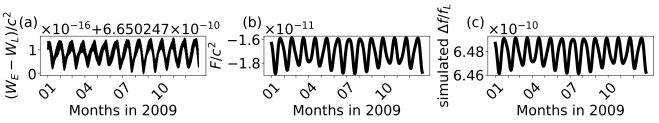

FIG. 5. Results for: (a) $(W_E - W_L)/c^2$ for the E-clock at APOLLO and L-clock at A15, (b) F/c^2 for the L-clock at A15, and (c) simulated $\Delta f/f_L$ for clocks at these locations, using 2009 data.

Conclusions and outlooks—As lunar clocks gain strategic importance for lunar timekeeping and chronometric geodesy, particularly given navigation plans and reference clock needs, modeling the Earth–Moon frequency link is timely and essential. This Letter simulates the fractional frequency differences between clocks assumed on Earth and the Moon, based on three key time transformations: the proper-to-coordinate time conversions for each clock (linked to local gravity potential) and the Earth–Moon coordinate time transformation. Two main parts are modeled in the frequency difference: the gravity potential difference term $(W_E - W_L)/c^2$ between the Earth and Moon clocks, and the Earth–Moon coordinate time ratio F/c^2. The latter distinguishes this work from clock comparisons within a single system like Earth's, where only the potential term applies.

To meet the 10^{-18} clock uncertainty, we assess each contribution to $(W_E - W_L)/c^2$ and F/c^2, retaining only those with effects larger than or near this level. For the Earth clocks, the gravity potential includes contributions from daily gravity field variations from GRACE-based modeling (incorporating both static and non-tidal components), solid Earth tides, pole tides, ocean tide loading, GNSS-derived surface deformation, atmosphere–ocean mass variability, and Earth's self-rotation. For the Moon clocks, we adopt the GL0900D lunar gravity model for higher accuracy, and include tidal potentials from Earth and Sun (up to degrees 3 and 2), degree-2 lunar Love numbers, and the effect of lunar self-rotation. With these contributions modeled, $(W_E - W_L)/c^2$ reaches the 10^{-10} level. F/c^2 is on the order of 10^{-11}, dominated by the Earth, Moon, and Sun, with smaller effects from Jupiter, Venus, and other planets. Two methods for calculating F/c^2 agree at the 10^{-18} level, mutually validating the result.

In our solution, LLR contributes significantly to lunar analysis and coordinate time ratio evaluation. Future developments may enable synergy between LLR and lunar clocks.

Acknowledgments—Current LLR data were collected, archived, and distributed under the auspices of the International Laser Ranging Service (ILRS; [51]). We gratefully acknowledge the efforts of personnel at the McDonald Observatory in Texas, USA, the LURE Observatory in Maui, Hawaii, USA, the Observatoire de la Côte d'Azur in France, the Wettzell Laser Ranging System in Germany, the Matera Laser Ranging station in Italy, and the Apache Point Observatory in New Mexico, USA, for obtaining LLR data since 1969. The authors also acknowledge the Deutsche Forschungsgemeinschaft (DFG, German Research Foundation) under Germany's Excellence Strategy-EXC-2123 QuantumFrontiers – Project-ID 390837967 and the SFB 1464 TerraQ – Project-ID 434617780.

[1] A. Bjerhammar, Bulletin Géodésique **59**, 207 (1985).
[2] A. Bjerhammar, *Relativistic Geodesy*, Tech. Rep. NOAA Technical Report NOS 118 NGS 36 (U.S. Dept. of Commerce, National Oceanic and Atmospheric Administration, National Ocean Service, Charting and Geodetic Services, Rockville, MD, 1986) accessed: 2025-01-13.
[3] C. Voigt, H. Denker, and L. Timmen, Metrologia **53**, 1365 (2016).
[4] S. Schröder, S. Stellmer, and J. Kusche, Geophysical Journal International **226**, 764 (2021), https://academic.oup.com/gji/article-pdf/226/2/764/37889131/ggab132.pdf.
[5] A. Vincent and J. Müller, Advances in Space Research **73**, 3312 (2024).
[6] A. Vincent and J. Müller, Vision of a clock-based network for absolute sea level monitoring (Springer Berlin Heidelberg, Berlin, Heidelberg, 2024) pp. 1–8.
[7] H. Wu, J. Müller, and C. Lämmerzahl, Geophysical Journal International **216**, 1594 (2018), https://academic.oup.com/gji/article-pdf/216/3/1594/27226427/ggy508.pdf.
[8] H. Wu and J. Müller, in *Beyond 100: The Next Century in Geodesy*, edited by J. T. Freymueller and L. Sánchez (Springer International Publishing, Cham, 2022) pp. 3–10.
[9] S. KC, Z. Shen, and W.-B. Shen, Geodesy and Geodynamics https://doi.org/10.1016/j.geog.2024.04.005 (2024).
[10] C. Qin, Y. Tan, and C. Shao, Physics Letters B **820**, 136471 (2021).
[11] S. Giuliani, B. D. Tapley, and J. C. Ries, Journal of Geodesy **98**, 50 (2024).
[12] European Space Agency, ESA's Moonlight programme: Pioneering the path for lunar exploration (2024), accessed: 2025-01-13.
[13] N. Speciale, L. Mann, J. Verville, N. Babu, and S. Sharma, Lunar relay services requirements document (srd) (2022), approved by Dave Israel and Jaime Esper on December 14, 2022.
[14] E. Gibney, Nature **614**, 13 (2023).
[15] N. Ashby and B. R. Patla, The Astronomical Journal **168**, 112 (2024).
[16] S. M. Kopeikin and G. H. Kaplan, Phys. Rev. D **110**, 084047 (2024).
[17] S. G. Turyshev, J. G. Williams, D. H. Boggs, and R. S. Park, The Astrophysical Journal **985**, 140 (2025).
[18] H. Denker, L. Timmen, C. Voigt, S. Weyers, E. Peik, H. S. Margolis, P. Delva, P. Wolf, and G. Petit, Journal of Geodesy **92**, 487 (2018).
[19] J. Müller, D. Dirkx, S. M. Kopeikin, G. Lion, I. Panet, G. Petit, and P. N. Visser, Space Science Reviews **214**, 1 (2018).
[20] G. Petit and B. Luzum, *IERS conventions (2010)*, Tech. Rep. (Bureau International des Poids et mesures sevres (france), 2010).
[21] A. Einstein, Jahrbuch der Radioaktivität und Elektronik **4**, 411 (1908).
[22] R. V. Pound and G. A. Rebka, Phys. Rev. Lett. **3**, 439 (1959).
[23] S. Kopeikin, M. Efroimsky, and G. Kaplan, *Relativistic Celestial Mechanics of the Solar System* (Viley-VCH Verlag, Weinheim, Germany, 2011).
[24] T. Liu, C.-G. Qin, J.-H. Pu, Y.-Z. Yang, and W.-B. Wang, Classical and Quantum Gravity **42**, 065016 (2025).
[25] W. McGrew, X. Zhang, R. Fasano, S. Schäffer, K. Beloy, D. Nicolodi, R. Brown, N. Hinkley, G. Milani, M. Schioppo, *et al.*, Nature **564**, 87 (2018).
[26] J. Grotti, I. Nosske, S. Koller, S. Herbers, H. Denker, L. Timmen, G. Vishnyakova, G. Grosche, T. Waterholter, A. Kuhl, S. Koke, E. Benkler, M. Giunta, L. Maisenbacher, A. Matveev, S. Dörscher, R. Schwarz, A. Al-Masoudi, T. Hänsch, T. Udem, R. Holzwarth, and C. Lisdat, Phys. Rev. Appl. **21**, L061001 (2024).
[27] B. Hofmann-Wellenhof and H. Moritz, *Physical geodesy* (Springer Science & Business Media, 2006).
[28] W. Farrell, Reviews of Geophysics **10**, 761 (1972).
[29] A. E. H. Love, *Some Problems of Geodynamics: Being an Essay to which the Adams Prize in the University of Cambridge was Adjudged in 1911* (University Press, 1911).
[30] T. Mayer-Gürr, S. Behzadpur, M. Ellmer, A. Kvas, B. Klinger, S. Strasser, and N. Zehentner, ITSG-Grace2018 - Monthly, Daily and Static Gravity Field Solutions from GRACE (2018).
[31] A. Kvas, S. Behzadpour, M. Ellmer, B. Klinger, S. Strasser, N. Zehentner, and T. Mayer-Gürr, Journal of Geophysical Research: Solid Earth **124**, 9332 (2019).
[32] L. Shihora, K. Balidakis, R. Dill, C. Dahle, K. Ghobadi-Far, J. Bonin, and H. Dobslaw, Journal of Geophysical Research: Solid Earth **127**, e2022JB024360 (2022).
[33] G. Blewitt, W. Hammond, and C. Kreemer, Eos **99**, e2020943118 (2018).
[34] RESIF, RESIF-RENAG French National Geodetic Network (2017), available at `http://renag.resif.fr/`.
[35] U. Community, PBO GPS Network - P027-ApachePnt_NM2007 P.S. (2007), available at `https://www.unavco.org/data/doi/search/search.html`.
[36] H.-G. Wenzel, Bull. Inf. Marées Terrestres **124**, 9425 (1996).
[37] D. C. Agnew, *SPOTL: Some Programs for Ocean-Tide Loading*, Tech. Rep. (UC San Diego: Scripps Institution of Oceanography, 2012) retrieved from `https://escholarship.org/uc/item/954322pg`.
[38] D. C. Agnew, Journal of geophysical research: solid earth **102**, 5109 (1997).
[39] C. Bizouard, S. Lambert, C. Gattano, O. Becker, and J.-Y. Richard, Journal of Geodesy **93**, 621 (2019).
[40] D. Kahan, F. G. Lemoine, A. S. Konopliv, and S. Goossens, Grail mission gravity model bundle (2022).
[41] R. B. Roncoli and K. K. Fujii, in *AIAA/AAS Astrodynamics Specialist Conference* (American Institute of Aeronautics and Astronautics, 2010).
[42] H.-G. Wenzel, Tide-generating potential for the earth, in *Tidal Phenomena*, edited by H. Wilhelm, W. Zürn, and H.-G. Wenzel (Springer Berlin Heidelberg, Berlin, Heidelberg, 1997) pp. 9–26.
[43] R. S. Park, W. M. Folkner, J. G. Williams, and D. H. Boggs, The Astronomical Journal **161**, 105 (2021).
[44] M. Zhang, *Characteristics and Benefits of Differential Lunar Laser Ranging*, Ph.D. thesis, Fachrichtung Geodäsie und Geoinformatik der Leibniz Universität Hannover (2023).
[45] V. V. Singh, *Lunar Laser Ranging - Improved Modelling and Parameter Estimation*, Ph.D. thesis, Fachrich-

tung Geodäsie und Geoinformatik der Leibniz Universität Hannover (2023).
[46] J. Müller, T. W. Murphy, U. Schreiber, P. J. Shelus, J.-M. Torre, J. G. Williams, D. H. Boggs, S. Bouquillon, A. Bourgoin, and F. Hofmann, Journal of Geodesy **93**, 2195 (2019).
[47] F. Hofmann, *Lunar laser ranging-verbesserte Modellierung der Monddynamik und Schätzung relativistischer parameter*, Ph.D. thesis, Fachrichtung Geodäsie und Geoinformatik der Leibniz Universität Hannover (2017).
[48] L. Biskupek, *Bestimmung der Erdorientierung mit Lunar Laser Ranging*, Ph.D. thesis, Fachrichtung Geodäsie und Geoinformatik der Leibniz Universität Hannover (2015).
[49] W. M. Folkner, J. G. Williams, D. H. Boggs, R. S. Park, and P. Kuchynka, Interplanetary Network Progress Report **196** (2014).
[50] S. A. Klioner, Astronomy & Astrophysics **478**, 951 (2008).
[51] M. R. Pearlman, C. E. Noll, E. C. Pavlis, F. G. Lemoine, L. Combrink, J. J. Degnan, G. Kirchner, and U. Schreiber, Journal of Geodesy **93**, 2161 (2019).